



Prediction method and research on characteristics of surface subsidence due to mining deeply buried Jurassic coal seams

Hejian Yin^{1,2} · Guangli Guo^{1,2} · Huaizhan Li^{1,2} · Tiening Wang^{1,2} · Yafei Yuan^{1,2}

Received: 20 May 2022 / Accepted: 17 September 2022 / Published online: 27 September 2022
© Springer-Verlag GmbH Germany, part of Springer Nature 2022

Abstract

Jurassic coal seams are a common geological feature in the mining areas of western China. Deeply buried Jurassic coal seams were mined in the Hujerte mining area in western China. The Hujerte mining area has a mining depth of more than 600 m, and the alluvium in the mining area is primarily composed of eolian sand. Understanding the characteristics of mining subsidence is crucial for preserving the ecological environment of the mining area. Surface subsidence caused by coal mining has different characteristics depending on geological conditions. However, the characteristics of surface subsidence caused by mining deeply buried Jurassic coal seams have rarely been studied. Therefore, using a coal mine in the Hujerte mining area as an example, the observed data of surface movements in the mining area are analyzed in this study. The results reveal that (1) when the ratio of mining width to depth are 0.44, 0.88, and 1.31, the subsidence factors are 0.129, 0.427, and 0.429, respectively, and (2) although the mining degree of the study area is larger than that of some coal mines in the eastern and western regions of China, the subsidence factor of the study area is still lower than that of these coal mines. Moreover, this study proposes a method for predicting the surface subsidence based on the T-distribution. At the edge of a subsidence basin, the fitting accuracy of the model is better than that of the probability integration method.

Keywords Jurassic coal seams · Eolian sand · Characteristics · Surface subsidence · Prediction method

Introduction

The western mining area of China has large coal reserves (Liu et al. 2019). As coal resources in the eastern region are depleted, the western region will be China's main coal production area in the future (Chen et al. 2019). The Shendong and Shanbei coal bases are important coal resource development bases in the mining area of western China (Xu et al. 2021). They are located in the border areas of China's Inner Mongolia and Shaanxi provinces. Originally, China primarily mined shallow Jurassic coal seams in these two

coal bases (mining depth of approximately 50–420 m). In view of the growing energy demand, the development of shallow-buried Jurassic coalfields is incapable of meeting the society's demands. Therefore, China planned a Hujerte mining area in the Shendong coal base. The Hujerte mining area is located in the Mu Us desert, and the alluvium is primarily composed of eolian sand. Deep Jurassic coal seams are mined in the mining area (mining depth over 600 m); the strata of the mining area consist primarily of Jurassic–Cretaceous layers.

Coal mining can cause severe ground subsidence. Mining-induced subsidence can lead to the destruction of cultivated land, buildings and structures, and groundwater resources (Finkelman and Tian 2018; Fernandez et al. 2020; Ghabraie et al. 2017; Kwinta and Gradka 2020; Salmi et al. 2017; Tajdus et al. 2018; Wang et al. 2021). Studying the characteristics of mining subsidence is crucial for protecting the ecological environment of a mining area. To understand the characteristics of mining subsidence, China has already established numerous surface movement observation stations in the central and eastern mining areas (Chi 2021; Hu et al. 2017; Li 2012; Wu 2015; Xie 2015). Based on the

✉ Guangli Guo
guangliguo@cumt.edu.cn

Hejian Yin
Yin_hj@cumt.edu.cn

¹ Jiangsu Key Laboratory of Resources and Environment Information Engineering, China University of Mining and Technology, Xuzhou 221116, Jiangsu, China

² School of Environment Science and Spatial Informatics, China University of Mining and Technology, Xuzhou 221116, Jiangsu, China

measured data, the subsidence factor, boundary angle, and other parameters describing the characteristics of mining subsidence are determined. These parameters can be used to guide the rational mining of coal to avoid surface damage caused by mining. In addition, mining subsidence prediction methods have been proposed by scientists to evaluate mining damage. Surface subsidence prediction methods include the influence function method (Li et al. 2014; Zhang et al. 2020), mechanical methods (Guo et al. 2016, 2020), and numerical simulation methods (Li et al. 2019; Gong and Guo 2019). In summary, mastering the characteristics of mining subsidence and building a subsidence prediction model are key to the scientific management of coal mining.

Studies have reported that the characteristics of mining subsidence change significantly when geological and mining conditions change significantly (Deng et al. 2014). The mining depth, mechanical strength of the overlying strata, and other factors are the most important factors influencing mining subsidence (Deng et al. 2014). For example, the greater the mining depth, the lower the surface subsidence under the same conditions (Deng et al. 2014); additionally, the harder the overburden, the lower the surface subsidence and the greater the height of the fractured water-conducting zone (Deng et al. 2014). The geological conditions of the Hujierite mining area differ significantly from those of the numerous mining areas in western China. For example, the mining depth of the Yushen and Shendong mining areas in western China is approximately 50–420 m. However, the mining depth of the Hujierite mining area is more than 600 m. In addition, the geological conditions of the Hujierite mining area are significantly different from those of the mining area in eastern China. For example, the alluvium in the Hujierite mining area is composed primarily of eolian sand, whereas the alluvium in the Huainan mining area in eastern China is composed primarily of clay. Therefore, the characteristics of mining subsidence in the Hujierite mining area may not be the same as those in the other mining areas. In the western region, scholars have studied the regularity of overlying rock mass and surface movement due to the mining of shallow Jurassic coalfields (Chen et al. 2019; Liu et al. 2019; Li 2017, 2020; Peng et al. 2015; Shen and Zhu 2019; Xu et al. 2021; Yan et al. 2018; Zhang and Liu 2015; Zhu 2019). However, the prediction methods and the characteristics of surface subsidence due to the mining of deeply buried Jurassic coal seams have rarely been studied. Accurate assessment of the extent of mining damage in the Hujierite mining area is challenging. Therefore, the prediction method and characteristics of surface subsidence caused by mining deeply buried Jurassic coal seams must be studied.

To address the abovementioned issues, herein, we conducted a case study in a coal mine in the Hujierite mining area. By processing the observed data of surface subsidence

in the study area, the characteristics of surface subsidence caused by mining deeply buried Jurassic coal seams were analyzed. Accordingly, a mathematical model suitable for predicting surface subsidence in the mining area was proposed. This study is organized as follows: “[Overview of the study area](#)” describes the geological and mining conditions in the study area, as well as the layout of the surface movement observation stations. “[Data processing methods](#)” describes the methods used to process subsidence data. “[Characteristics of mining subsidence](#)” describes the characteristics of mining subsidence in the study area and compares them with other mining areas. In addition, this section describes the shortcomings of the conventional subsidence prediction model for fitting subsidence data. “[A model for predicting surface subsidence based on the T-distribution](#)” describes a new ground subsidence prediction model. At the edge of the subsidence basin, the fitting accuracy of the model was found to be better than that of the conventional method. “[Conclusions](#)” provides the main results and limitations of this study.

Overview of the study area

Geological and mining conditions

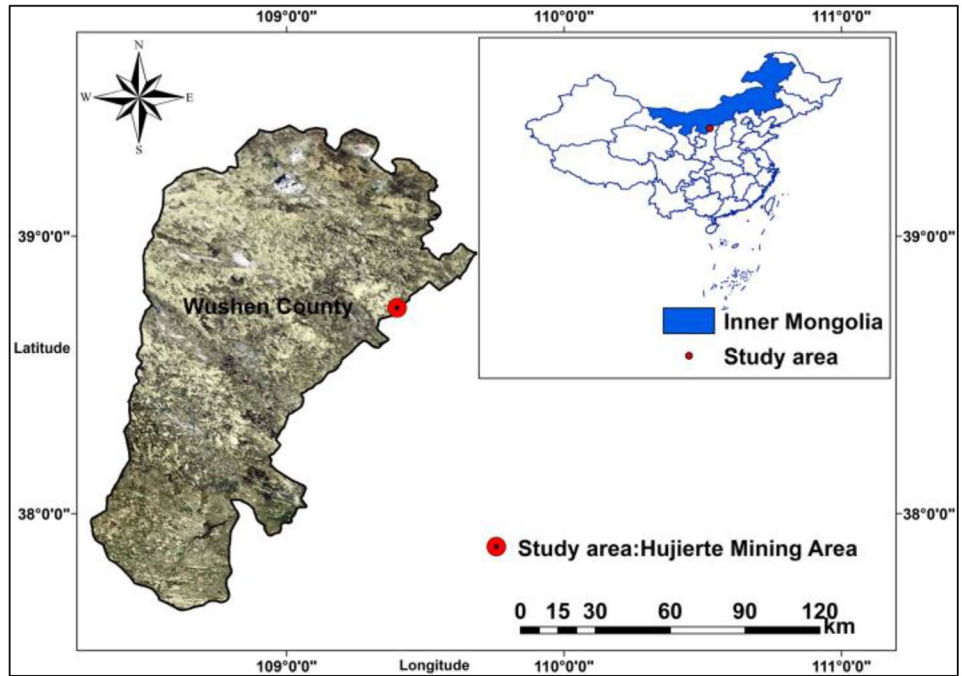
As shown in Fig. 1, the Hujierite mining area is located in the Wushen County, China. The mining area covers an area of 3331.7 km², and the coal reserves in the exploration area are 18,004.10 Mt. The Hujierite mining area was planned by the Chinese government in 2013. Only five coal mines have begun operation in the mining area, and the geological and mining conditions of these coal mines are similar. One of these coal mines was selected for this study.

The designed annual output of this coal mine is 4.0 Mt/year. In chronological order from oldest to youngest, the strata in the mining area are the Jurassic Yanan formation, Jurassic Zhiluo formation, Jurassic Anding formation, Cretaceous Zhidan formation, and Quaternary. The stratigraphic structure is simple and contains no igneous rock. The coal-bearing rock series is from the Jurassic Yanan formation. The 3–1 coal seam is the first coal seam to be mined; it is nearly horizontal, with an average thickness of 5.51 m and depth of the seam more than 600 m. District no. 11 was the first district to be excavated.

As can be seen in Fig. 2, the coal mine has arranged long-wall panels 101, 102, and 103, which are all adjacent, to the east of district no. 11. The width of the coal pillars between the two panels is 30 m, and their mining sequences are panels 101, 102, and 103. A generalized stratigraphic column exposed by a borehole is shown in Fig. 2. The geological and mining conditions of the panels are listed in Table 1.

As listed in Table 1, D_0 , L_0 , M , α , H , h , and C are the panel width, panel length, mining height, dip angle of the coal seam,

Fig. 1 Geographic location of the study area



average mining depth, average thickness of alluvium, and the panel advance rate, respectively. In Table 2, N is the number of particles; and c_1 and c_2 are the acceleration constants.

The geological and mining conditions in the mining area have the following characteristics, as presented in Table 1 and Fig. 2. (1) The coal seam is buried deep and is nearly horizontal. (2) The alluvium is composed primarily of eolian sand, with an average thickness of 128 m. (3) The rock mechanical strength of the Cretaceous strata is generally soft, whereas that of the Jurassic strata, which is composed predominantly of sandstone with medium-hard strength, is typically greater than 30 MPa. In addition, the fully mechanized full-seam coal mining technology is used for mining, whereas a caving method is used to treat the roof.

The surface movement observation station

Two observation lines (lines A and B) were established at locations approximately 714 m and 1531 m from the open-off cut of panel 102, as shown in Fig. 2. The length of observation line A was 1275 m, and it contained 41 observation points with an average spacing of 31 m, marked as A_1, A_2, \dots, A_{41} . The length of observation line B was 2184 m, and it contained 66 observation points with an average spacing of 33 m, marked as B_1, B_2, \dots, B_{66} . A level was used to observe the elevation data at each point in the coal mine. These points were first observed in the coal mine before panel 101 was advanced. During the observation period, some observation sites were damaged by residents. Therefore, some observation data were missing.

Data processing methods

First, the subsidence values were calculated for each point on the observation line. Second, the boundary angle of the observation line was calculated. Note that boundary angle is an important parameter for measuring the scope of a subsidence basin.

As shown in Fig. 3, this study defines the boundary angle as the angle between the line connecting the point with 10 mm of subsidence on the observation line to the boundary of the gob, and the horizontal line on the side of the coal pillar. Herein, γ is the boundary angle on the rise and β is the boundary angle on the dip.

Finally, the parameters of the probability integration method were inverted.

Probability integration method (PIM) is a prediction method for surface subsidence; it is widely used in China. A detailed introduction to the principle of PIM can be found in Deng et al. (2014). The center of a rectangular longwall panel serves as the origin, and the X - and Y -axes point to the strike and dip of the coal seam, respectively. Thus, the formula $W_{pim}(x, y)$ to calculate the subsidence of any point (x, y) on the surface based on the PIM can be expressed by Eq. (1) (Deng et al. 2014):

$$W_{pim}(x, y) = \frac{1}{W_{max}} \left[W_{PIM} \left(x + \frac{l}{2} - s_{0y} \right) - W_{PIM} \left(x - \frac{l}{2} + s_{0z} \right) \right] \left[W_{PIM} \left(y - H \cot \theta_0 + \frac{L}{2} - DS_{02} \right) - W_{PIM} \left(y - H \cot \theta_0 - \frac{L}{2} + DS_{01} \right) \right], \tag{1}$$

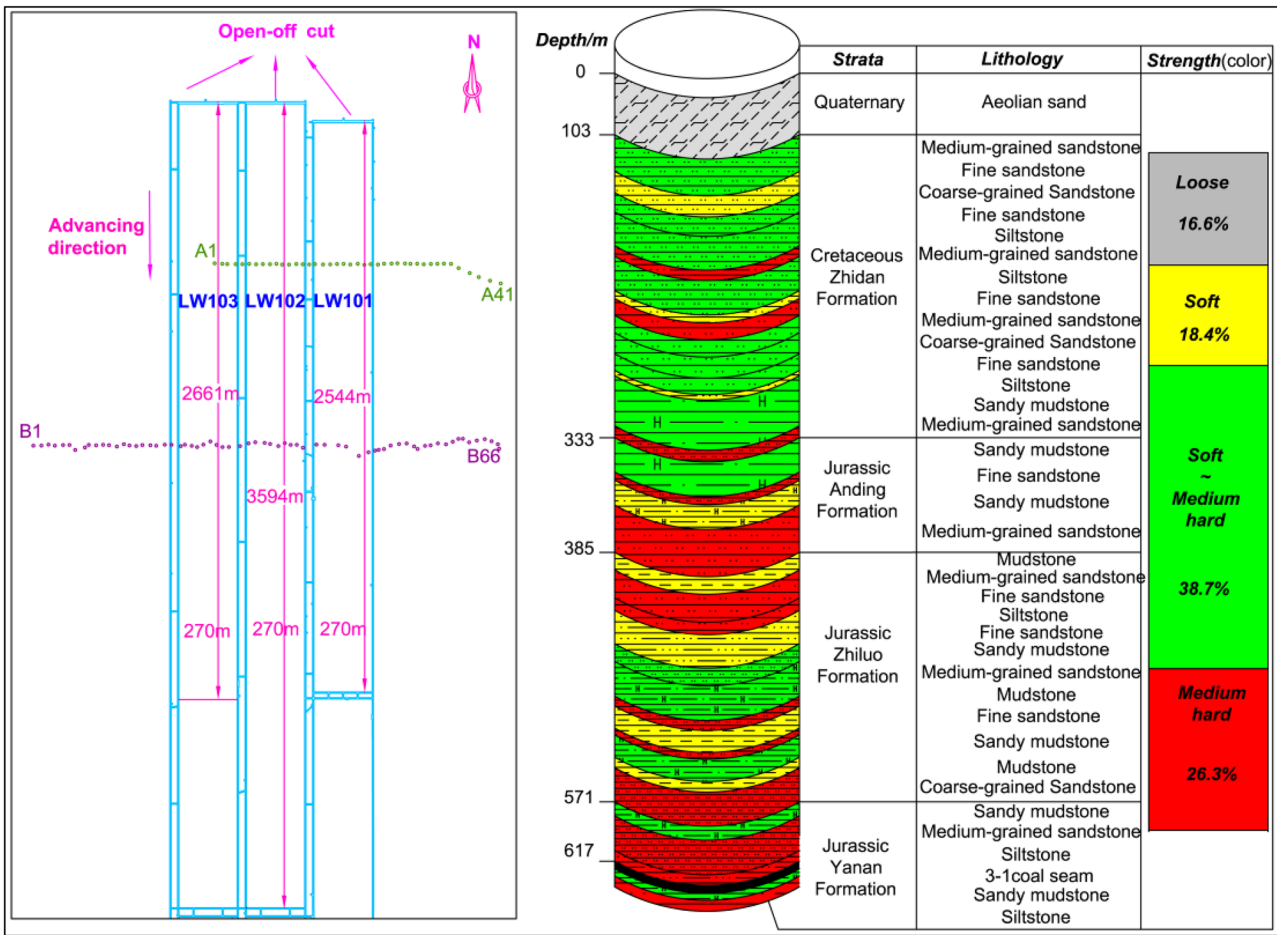


Fig. 2 Relative positions of the three panels and stratigraphic features

where $W_{PIM}(x)$ and $W_{PIM}(y)$ indicate the prediction equation for the surface subsidence when the scope of the excavation area is semi-infinite along the strike and dip of the coal seam, respectively (Deng et al. 2014); l and L indicate the computational length of the panel along the strike and dip of the coal seam (m), respectively; and s_{0z} and s_{0y} denote the deviation of the inflection point along the left and right sides of the coal seam (m), respectively, and are parameters of PIM.

Note that $W_{pim}(x, y)$ consists of a W_{PIM} , which is described as follows:

$$W_{PIM} = \frac{W_{max}}{2} \left(1 + erf \left(\frac{x\sqrt{\pi}}{r_p} \right) \right), \tag{2}$$

where r_p is the main influence radius (m); and W_{max} indicates the maximum subsidence value (mm), whose calculation method is as follows:

$$W_{max} = Mq_0 \cos\alpha, \tag{3}$$

where q_0 indicates the subsidence factor and is an essential parameter of PIM; M is the mining height (mm); and α is the dip angle of the coal seam ($^\circ$).

In addition, the calculation for r_p in Eq. (2) is as follows:

$$r_p = \frac{H}{\tan\beta_0}, \tag{4}$$

Table 1 Geological and mining conditions of panels

Panel	D_0 (m)	L_0 (m)	M (m)	α ($^\circ$)	H (m)	h (m)	C (m/d)
101	270	2544	5.4	1.5	615	100	10
102	270	3594	5.4	1.5	615	121	10
103	270	2661	5.5	1.5	636	162	10

Table 2 Parameters of the PSO

G	N	ω_{max}	ω_{min}	c_1	c_2
600	600	0.9	0.4	1	1

where $\tan\beta_0$, which is a parameter of PIM, denotes the tangent of main influence angle.

The relationship between the computational length L and the actual length D (m) of the panel along the dip of the coal seam is as follows:

$$L = \frac{D \sin(\alpha + \theta_0)}{\sin\theta_0}, \tag{5}$$

where θ_0 , which is another parameter of PIM, denotes the influence transference angle.

In Eq. (1), the expressions for DS_{01} and DS_{02} are as follows:

$$DS_{01} = \frac{s_{01} \sin(\alpha + \theta_0)}{\sin\theta_0}, \tag{6}$$

$$DS_{02} = \frac{s_{02} \sin(\alpha + \theta_0)}{\sin\theta_0}, \tag{7}$$

where s_{01} and s_{02} indicate the deviation of the inflection point along the dip and rise sides of the coal seam (m), respectively, and are parameters of the PIM.

The PIM parameter reflects the surface subsidence characteristics of the mining area. For example, the subsidence factor and the tangent of main influence angle can reflect the degree of surface subsidence and the morphological characteristics of the subsidence curve in the mining area, respectively. In general, the subsidence factor decreases as surface subsidence decreases. Essentially, the flatter the subsidence curve, the smaller the tangent of main influence angle. Therefore, in this study, the PIM parameters were used to describe the characteristics of the mining subsidence in the study area.

Particle swarm optimization (PSO) is a common method for inverting the PIM parameters. Detailed descriptions on

PSO can be found in the literature (Wen 2015). Owing to space limitations, the method is not discussed in detail in this study. PSO uses a fixed inertia weight, which is inconvenient for determining an optimal solution (Cai et al. 2022). Therefore, an adaptive particle swarm algorithm (APSO) was used in this study to invert the PIM parameters. The APSO can perform nonlinear adaptive adjustments to the inertial weight according to Eq. (8) (Cai et al. 2022).

$$\omega = \omega_{max} - (\omega_{max} - \omega_{min}) \left(\frac{ps_{o_{iter}}}{G} \right)^2, \tag{8}$$

where ω_{max} and ω_{min} are the maximum and minimum values of the inertia weight, respectively; $ps_{o_{iter}}$ is the current number of iterations; and G is the maximum number of iterations of the APSO.

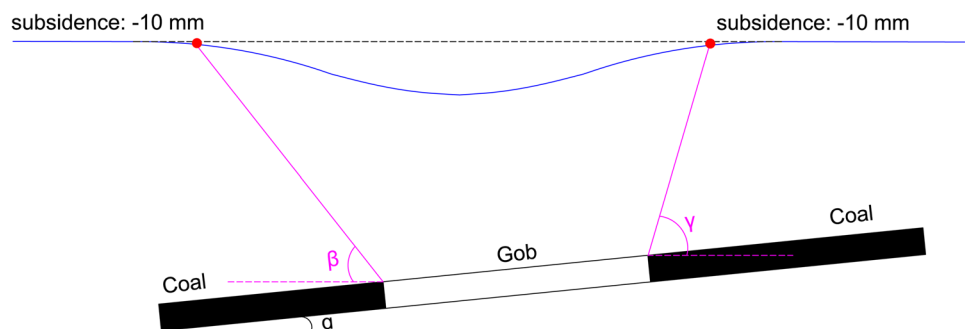
Characteristics of mining subsidence

Regularity of the surface subsidence

The ratio between the excavation width and depth in district no. 11 is defined as R . As shown in Fig. 2, when panel 101 was advanced, $R=0.44$. When panel 102 was advanced, $R=0.88$. When panel 103 was advanced, $R=1.31$. The terminal mining line of the longwall panel was far from the observation line (more than 1100 m away). When the advancing position of each panel was close to the terminal mining line, the propagation of the mining subsidence to the observation line was difficult. When each panel completed its advance, the maximum subsidence velocity of the surface was less than 0.9 mm/day. The subsidence of the observation point essentially came to a halt. The surface subsidence curves with different values of R are shown in Fig. 4.

As can be seen in Fig. 4, the surface subsidence curve became flatter when the first panel finished advancing ($R=0.44$). The surface subsidence values were small, and the maximum subsidence values of lines A and B were -188 and -201 mm, respectively. When panel 102 finished advancing ($R=0.88$), the subsidence values of lines A and B

Fig. 3 Definition of the boundary angle



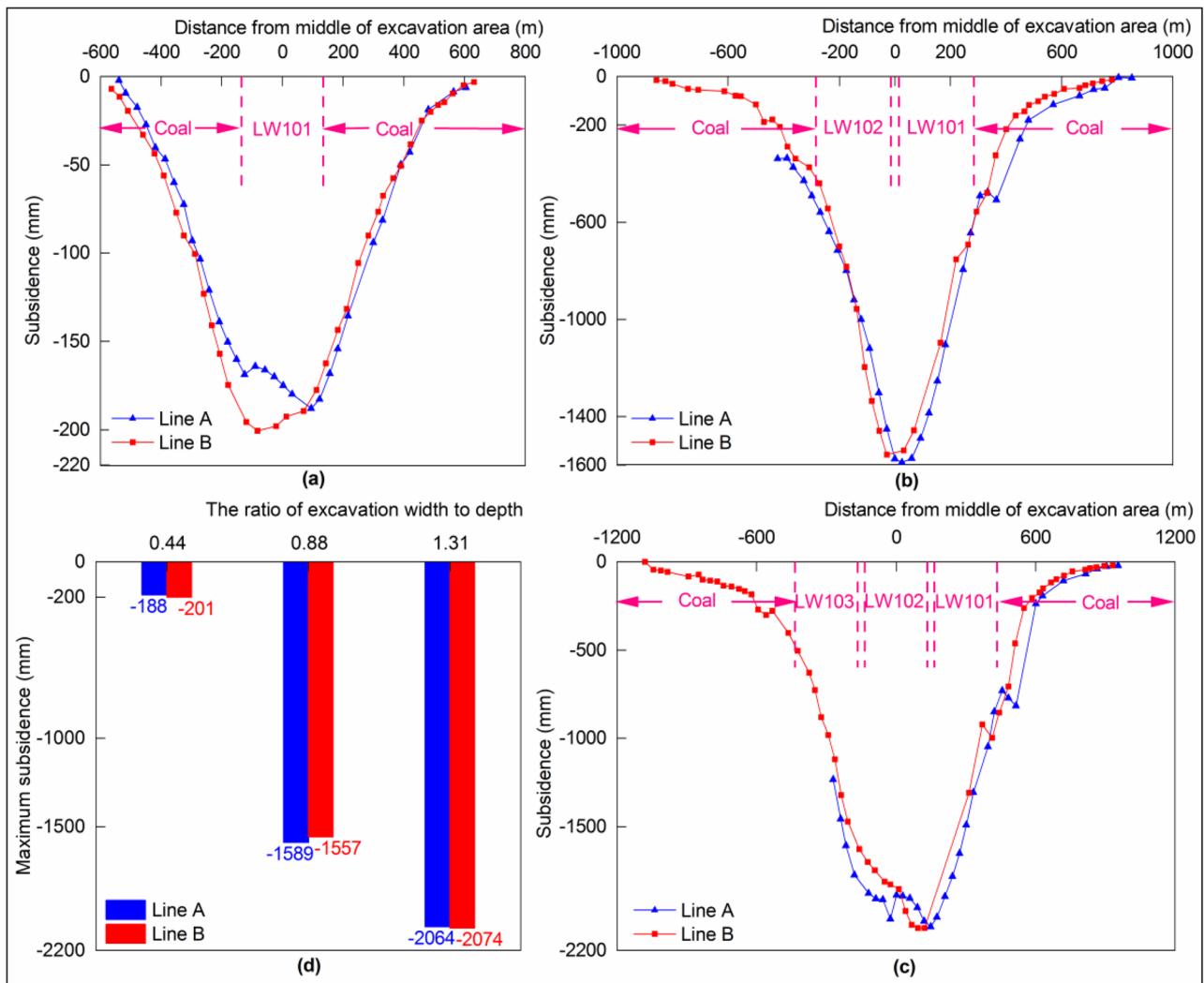


Fig. 4 Surface subsidence curves with different R values of a $R=0.44$, b $R=0.88$, and c $R=1.31$, d maximum subsidence

increased significantly. The maximum subsidence values of the two lines were -1589 and -1557 mm, corresponding to an increase of 8.46 and 7.75 times, respectively. When panel 103 finished advancing ($R=1.31$), the maximum subsidence values of the two lines were -2064 and -2074 mm, corresponding to increases of 29.9% and 33.3%, respectively. At this point, the magnitude of the increase in subsidence decreased.

Boundary angle of the subsidence basin

Next, the characteristics of the boundary angles were analyzed. The boundary angles of each observation line for the different values of R are listed in Table 3.

As presented in Table 3, the boundary angle decreased with increasing R . When R increased from 0.44 to 0.88, the boundary angle β of line B decreased from 56.2 to 46.4° , i.e., by 9.8° . As R increased from 0.88 to 1.31, the boundary angle β

of line B decreased by 1.4° . Thus, when panel 102 completed its advance, the scope of the subsidence basin increased significantly. When panel 103 completed its advance, the extent of the subsidence basin enlargement decreased.

Fitting effect of surface subsidence based on PIM

A comparison between the predicted subsidence values based on the PIM and the measured values is shown in Fig. 5. In mining subsidence engineering, the relative error RE is

Table 3 Boundary angle ($^\circ$)

R	Line A		Line B	
	Γ	β	γ	β
0.44	55.6	58.5	55.4	56.2
0.88	50.1	/	50.2	46.4
1.31	48.4	/	49.3	45.0

typically used to evaluate the fitting effect (%). $RE = m_w / W_{max}$, where m_w is the root mean square error (mm) and W_{max} is the maximum subsidence (mm). According to the calculation results, when $R = 0.44, 0.88, \text{ and } 1.31$, the RE values were 4.6, 5.2, and 4.6%, respectively.

In the mining area, the fitting accuracy of the PIM was less than 6% and the fitting effect was good. However, PIM

has certain shortcomings. As shown in Fig. 5c–f, the extent of the subsidence basin was large when R was greater than or equal to 0.88. The surface subsidence curve had the characteristics of a long-tailed distribution. At this point, the fitting accuracy of PIM at the edge of the subsidence basin was poor. Chinese engineers commonly use PIM to predict the boundary of the subsidence basin. Therefore, accurately

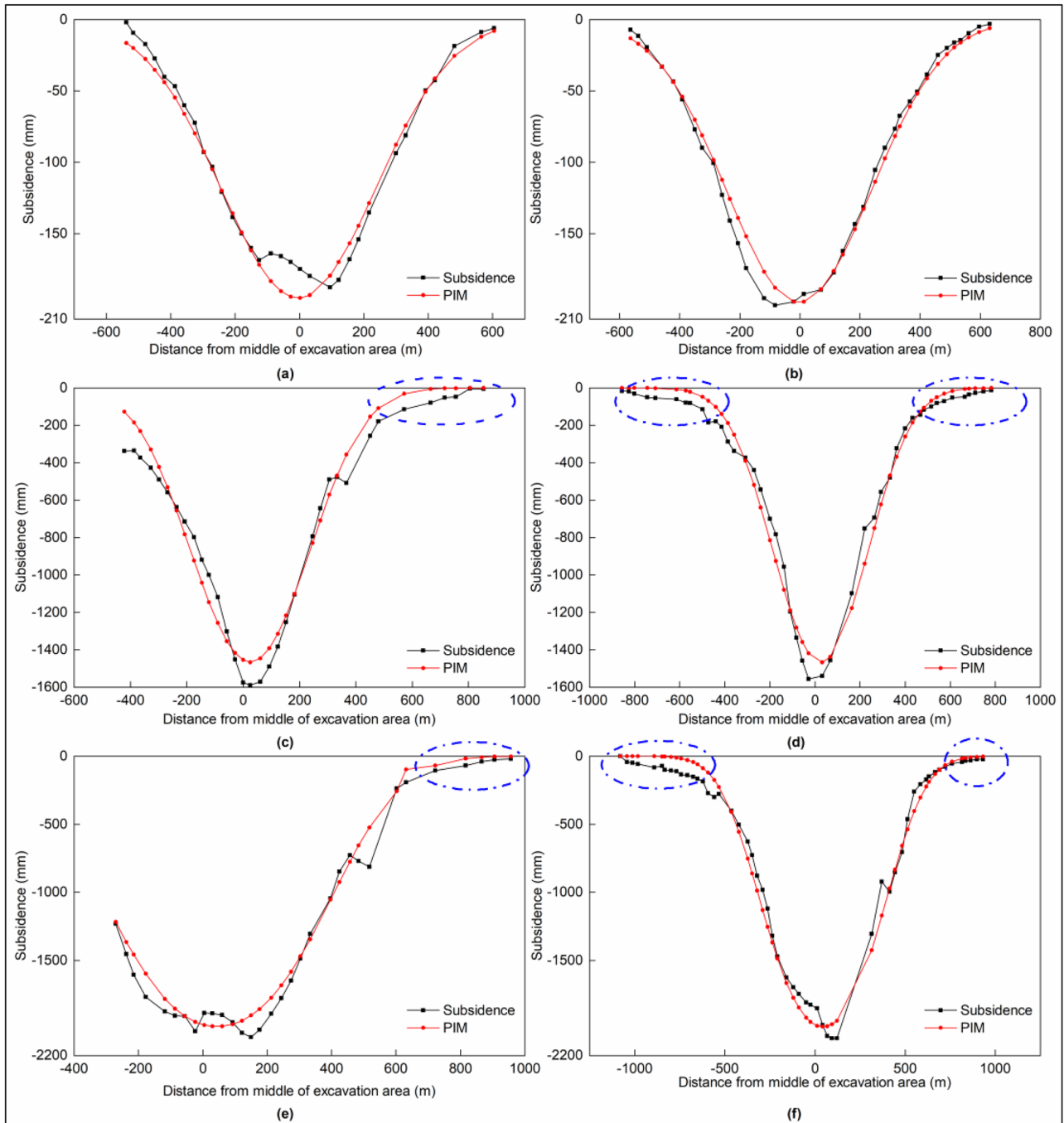


Fig. 5 Fitting effect of PIM when **a** $R = 0.44$ for line A, **b** $R = 0.44$ for line B, **c** $R = 0.88$ for line A, **d** $R = 0.88$ for line B, **e** $R = 1.31$ for line A, and **f** $R = 1.31$ for line B

Table 4 Parameters of PIM for the study area

R	q_0	$\tan\beta_0$	θ_0 (°)	s_{0z} (m)	s_{0y} (m)	s_{01} (m)	s_{02} (m)
0.44	0.129	1.056	90	130	96	46	53
0.88	0.427	1.468	90	8	82	130	86
1.31	0.429	1.400	90	6	55	130	48

predicting the boundaries of mining-induced damage in the Hujierite mining area using PIM is not possible.

Characteristics of the parameters of PIM

The parameters obtained by inversion are listed in Table 4.

As presented in Table 4, when panel 101 finished advancing (when $R=0.44$), q_0 was very small (less than 0.13). q_0 increased significantly after panel 102 finished advancing ($R=0.88$); at this point, $\tan\beta_0$ also increased.

Chinese engineers classify the overlying strata into three types (Hu et al. 2017): hard (uniaxial compressive strength of more than 60 MPa), medium hard (uniaxial compressive strength of 30–60 MPa), and soft (uniaxial compressive strength of less than 30 MPa). The greater the mechanical strength of the overlying strata, the smaller the subsidence factor and the tangent of main influence angle. According to the literature (Hu et al. 2017), q_0 and $\tan\beta_0$ are generally less than 0.55 and 1.92, respectively, during coal mining under conditions of hard overlying strata. Therefore, when R is less than or equal to 1.31, the regularity of surface subsidence in the study area exhibits partial characteristics of surface subsidence during mining under hard overlying strata

conditions. After panel 101 completed its advance, the ratio between the height of the fractured water-conducting zone and the mining height was 23.4 (Yang et al. 2019). According to the literature, this ratio is typically greater than 18 for coal mining under hard overlying strata (Hu et al. 2017). Thus, the obtained results further indicate that the regularity of surface subsidence and overlying strata movement in the Hujierite mining area exhibits partial characteristics of surface subsidence during mining under hard overlying strata conditions.

Deep Jurassic coal seam is mined in the Hujierite mining area. However, the western region contains numerous mining areas where Jurassic coal seams are mined at shallow depths (e.g., the Huojitu and Bulianta coal mines in the Shendong mining area, the Chahasu coal mine in the Xinjie mining area, and the Yushuwan and Longde coal mines in the Yushen mining area). The mining depth of these areas is approximately 70–418 m, and the mechanical strength of the overlying strata is medium-hard. As shown in Fig. 6, these mining areas are adjacent to the Hujierite mining area. The geological and mining conditions of some panels of these coal mines are listed in Table 5.

Fig. 6 Geographic location of coal mines in the mining area in western China

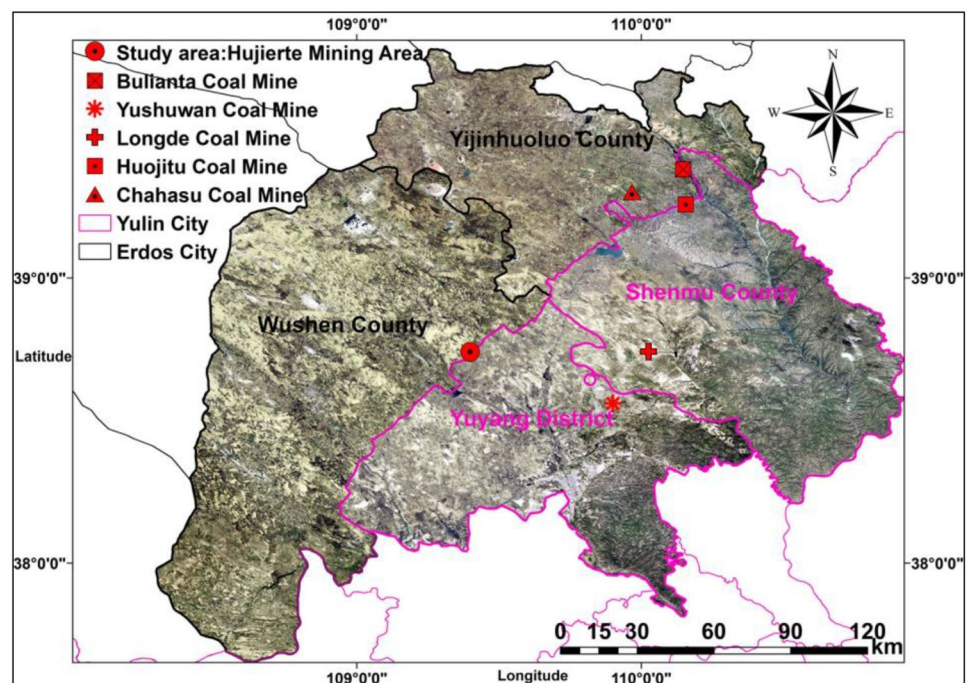


Table 5 Geological and mining conditions of some panels of other coal mines (Chen 2015; Chi 2021; Hu et al. 2017; Jia et al. 2019; Li 2012, 2017; Peng et al. 2015; Shen and Zhu 2019; Tao and Jia 2021; Wu 2015; Xie 2015; Zhang and Liu 2015; Zhu 2019)

Geographic locations	Coal mine-panel	M (m)	α (°)	h (m)	H (m)	C (m/d)	D_0 (m)	L_0 (m)	Alluvium
West	Huojitu 12,205	3.5	1.0	17	71	14.0	230	2251	A-L
West	Bulianta 31,401	4.2	1.5	18	241	16.0	266	4629	A-L
West	Yushuwan 20,101	5.0	1.5	156	270	4.0	250	3407	A-L
West	Chahasu 3101	4.6	1.5	11	418	8.9	301	2504	A-L
West	Longde 205	4.0	< 1	36	218	9.2	300	3640	A-L
Central	Xuehu 2102	2.8	12.0	386	722	—	156	466	C-S
East	Panyi 1252	2.7	6	165	802	3.2	260	1150	C-S
East	Zhujidong 1111(1)	1.8	3.0	278	920	4.2	230	1585	C-S
East	Tangkou 1301	3.4	5.0	212	1000	3.4	215	1320	C-S

A deep coal seam is mined in the Hujierte mining area. In central and eastern China, several mining areas (e.g., Xuehu coal mine in the Yongxia mining area, Panyi and Zhujidong coal mines in the Huainan mining area, and Tangkou coal mine in the Jining mining area) also mine deeply buried coal seams. These mining areas excavate Carboniferous–Permian coal seams at depths of more than 600 m. The overlying strata have a medium-hard mechanical strength. The geographical location of these mines is shown in Fig. 7, and the geological and mining conditions of some panels of these coal mines are listed in Table 5.

In Table 5, A-L indicates that the alluvium is composed primarily of eolian sand and loess, whereas C-S indicates that the alluvium is composed primarily of clay and sand layers.

A fully mechanized coal mining technology was used to excavate all the panels listed in Table 5. A caving method was used to treat the roofs. The data presented in Tables 1 and 5 reveal that the excavation size and advance rate in the mining area in western China were much larger than those in eastern China. Essentially, the mining intensity in the western China mining area is greater than in the eastern China mining area. Moreover, the alluvium in the western mining area contains less clay and consists primarily of eolian sand and loess.

To determine whether the subsidence characteristics of these mining areas are similar to those of the Hujierte mining area, the PIM parameters were compared with those of the study area. The PIM parameters for each panel are listed in Table 6.

As presented in Tables 4 and 6, although the mining degree of the study area was greater than that of some coal mines in the eastern and western regions of China, the q_0 of the study area was still less than that of the coal mines. The Hujierte mining area and some coal mines in eastern China excavate deeply buried coal deposits, and the mining intensity in the Hujierte mining area is higher. However, the q_0 of the Hujierte mining area was found to be much lower than that of some coal mines in eastern China. Thus, compared

with the mining of shallow Jurassic coal seams in western China and deep coal seams in eastern China, the subsidence in the Hujierte mining area is small. In addition, the tangent of main influence angle in the study area was smaller than that in other mining areas, which indicates that the surface subsidence curve in the Hujierte mining area is flatter in comparison.

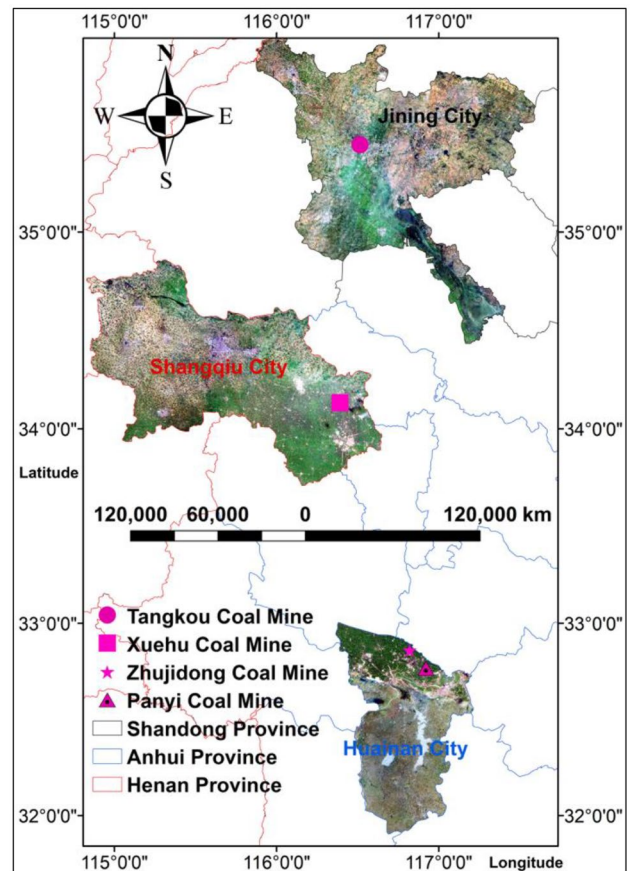


Fig. 7 Geographical location of coal mines in the mining area in central and eastern China

Table 6 Subsidence factor and the tangent of main influence angle in other mining areas (data in the table are from the literature in Table 5)

Location	Panel	R	q_0	$\tan\beta_0$
West	Huojitu 12205	3.24	0.73	1.98
West	Bulianta 31401	1.11	0.54	4.90
West	Yushuwan 20101	0.93	0.50	3.35
West	Chahasu 3101	0.72	0.80	4.67
West	Longde 205	1.38	0.60	2.00
Central	Xuehu 2102	0.22	0.87	1.78
East	Panyi 1252	0.33	0.75	1.80
East	Zhujidong 1111(1)	0.25	0.46	1.70
East	Tangkou 1301	0.22	0.52	2.15

Preliminary analysis of subsidence mechanism

The results presented in the previous section indicate that the surface subsidence in the Hujierite mining area is small. In this section, the mechanism of small surface subsidence in the mining area is analyzed.

A previous study reported that the lithology and thickness of the rock mass are the factors that influence the mining subsidence characteristics of the mining areas (Hu et al. 2017). To reveal the mechanism of the small surface subsidence in the study area, the characteristics of rock masses in the Hujierite mining area were investigated in this section. The characteristics of rock masses in the two types of typical mining areas were compared with those of the study area. One type of mining area is located in western China; herein, shallowly buried Jurassic coal seams are mined (e.g., the Bulianta coal mine in the Yushen mining area), whereas the other type of mining area is located in central

and eastern China, and mines deeply buried coal seams (e.g., the Xuehu coal mine in the Yongxia mining area).

Taking the study area, and the Bulianta and Xuehu coal mines as examples, the ratio of the total thickness of the rock mass with different lithologies to the height of the overlying rock mass was calculated based on their borehole columnar sections (Li 2012; Xu 2016), as shown in Fig. 8a. Furthermore, the ratio of the number of rock masses in different thickness ranges to the total number was calculated (see Fig. 8b).

As shown in Fig. 8, the lithology of the overlying strata in the study area and Bulianta coal mine was dominated by sandstone, which accounted for 60.3% and 60.1%, respectively. However, the percentage of mudstone was very low; in the study area, it was only 6.6%. In contrast, the proportion of mudstone in the Xuehu coal mine in the central regions was relatively large, accounting for 4.6 times that of the study area. The overlying strata of the study area contained thicker rock masses compared with the Bulianta and Xuehu coal mines; in the study area, rock masses thicker than 10 m accounted for 63.6%, which is 2.5 times the thickness of the Bulianta coal mine. In contrast, approximately 89.1% of the rock masses in the Xuehu coal mine had thickness in the range of 0–10 m. The Xuehu coal mine did not contain any rock masses with a thickness of more than 20 m.

In summary, the geological conditions of the Hujierite mining area have some distinct features compared with those of other mining areas: (1) The overlying strata are primarily sandstone; and (2) the overlying strata contain multiple layers of rock mass with large thicknesses and medium-hard mechanical strength.

Compared with the Shendong and Yushen mining areas, where the Jurassic coal seams are shallowly buried, the overlying layers of the Hujierite mining area primarily comprise multi-layer thick and medium-hard rock masses, as shown in

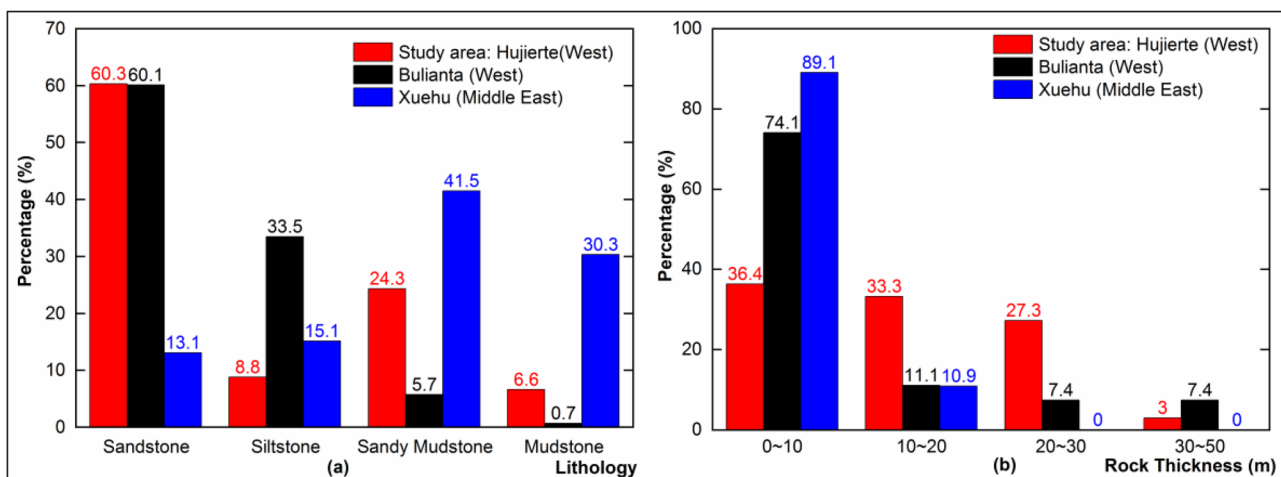


Fig. 8 Stratigraphic information in the study area, Bulianta coal mine, and Xuehu coal mine. **a** Proportion of the different lithologies; **b** proportion of the thickness of the rock mass

Fig. 8. They can be considered a key stratum controlling the movement of the strata. The subsidence factor and tangent of main influence angle in the Hujierite mining area are relatively small because the overlying strata are controlled by a multilayer of thick and medium-hard rock masses.

When the first panel of the Hujierite mining area had finished advancing, the height of the fractured water-conducting zone was 23.6 times the mining height. If the primary key stratum is located within the fractured water-conducting zone, the fissure of the primary key stratum passes through. According to the key stratum theory (Xu 2016), when the fissure of the primary key stratum passes through it, the fractured water-conducting zone develops toward the top of the overlying strata. However, in the Hujierite mining area, no fractured water-conducting zone develops on the top of the overlying strata, and the overlying strata of the mining area still contain a sagging zone. Therefore, the primary key stratum is not in the fractured water-conducting zone, and the distance (126 m) between its position and the coal seam is greater than 23.6 times the mining height. However, in the Shendong and Yushen mining areas, the distance between the primary key stratum and the coal seam is often less than 7–10 times the mining height (Xu 2016). Therefore, the distance between the primary key stratum and the coal seam is typically greater in the Hujierite mining area than that in the Shendong and Yushen mining areas. Under the same conditions, the farther the primary key stratum is from the coal seam, the smaller the surface subsidence. This is one reason why the subsidence factor of the Hujierite mining area is smaller than that in the Shendong and Yushen mining areas.

Compared with some coal mines in the mining areas in eastern China, where deeply buried coal deposits are extracted, the overlying strata in the Hujierite mining area contain more sandstone and less mudstone. In addition, each layer of rock mass is generally thicker in the Hujierite mining area. In contrast, in the eastern China mining area, the overlying strata contain more mudstones, and the thickness of the rock mass is small (typically 0–10 m). Compared with mudstone, sandstone is less susceptible to plastic deformation when subjected to an external force. Compared with the thin rock masses, the subsidence caused by mining is less in the thick rock masses. In addition, the alluvium in the mining area of eastern China contains numerous clay components. Therefore, the alluvium in the mining area in eastern China is susceptible to compression after mining disturbances. In the Hujierite mining area, the alluvium is composed primarily of eolian sand. Compared with clay, eolian sand is less susceptible to compression by external forces. Therefore, the subsidence factor in the Hujierite mining area is relatively low compared to that of some coal mines in eastern China.

A model for predicting surface subsidence based on the T-distribution

As shown in Fig. 5c–f, the fitting accuracy of PIM at the edge position of the subsidence basin was poor when $R \geq 0.88$. The improvement in the fitting accuracy of the edge position of the subsidence basin is conducive to the accurate prediction of the boundary of the mining-induced damage. Therefore, a new subsidence prediction model must be developed to improve the fitting accuracy of the edge position of the subsidence basin.

Prediction model

To further improve the accuracy of subsidence prediction, a prediction model of surface subsidence based on the T-distribution (ITM) was proposed in this study.

The probability density function (PDF) and cumulative distribution function (CDF) of the T-distribution are shown in Eqs. (9) and (10), respectively (Chen 2020; Moore et al. 2012).

$$f_T = \frac{\Gamma\left(\frac{n+1}{2}\right)}{\sigma\Gamma\left(n/2\right)\sqrt{n\pi}} \left[\frac{n + \left(\frac{x-\mu}{\sigma}\right)^2}{n} \right]^{-\frac{(n+1)}{2}} \sim T(\mu, \sigma^2, n), \quad (9)$$

$$F_T = \int_{-\infty}^x f_T dx = \frac{1}{2} + \frac{\left(\frac{x-\mu}{\sigma}\right)\Gamma\left(\frac{n+1}{2}\right)}{\Gamma\left(n/2\right)\sqrt{n\pi}} {}_2F_1\left(\frac{1}{2}, \frac{n+1}{2}; \frac{3}{2}; -\frac{(x-\mu)^2}{n\sigma^2}\right), \quad (10)$$

where $\Gamma(\cdot)$ is the gamma function; ${}_2F_1(\cdot)$ is the hypergeometric function; n is the degree of freedom, and $n > 0$; u is a location parameter; and σ is the scale parameter.

When $u = 0$, according to the properties of the continuous distribution function:

$$\begin{cases} \lim_{x \rightarrow -\infty} F_T = 0 \\ \lim_{x \rightarrow +\infty} F_T = 1 \\ F_T(x = 0) = \frac{1}{2} \end{cases}, \quad (11)$$

In fact, the function curves of F_T and W_{PIM} are both S-shaped. The derivation to relate Eq. (10) to Eq. (2) is as follows:

When the location parameter of the normal distribution is $u_n = 0$, its PDF and CDF are as follows (Fang and Xu 2016):

$$f_{PDF} = \frac{1}{\sqrt{2\pi}\sigma_n} \exp\left(-\frac{x^2}{2\sigma_n^2}\right), \quad (12)$$

$$f_{CDF} = \frac{1}{2} \left(1 + \operatorname{erf} \left(\frac{x}{\sigma_n \sqrt{2}} \right) \right). \tag{13}$$

The relationship between the influence function of the PIM and PDF of the normal distribution is:

$$w_{PIM} = \frac{1}{r_p} \exp \left(-\pi \left(\frac{x}{r_p} \right)^2 \right) \sim N \left(0, \left(\frac{r_p}{\sqrt{2\pi}} \right)^2 \right). \tag{14}$$

The scale parameter σ_n of the normal distribution was transformed as follows:

$$\sigma_n = r_p / \sqrt{2\pi} \tag{15}$$

Substituting Eq. (15) into Eq. (13), the CDF of the influence function of the PIM can be obtained as follows:

$$F_{PIM} = \int_{-\infty}^x w_{PIM} dx = \frac{1}{2} \left(1 + \operatorname{erf} \left(\frac{x\sqrt{\pi}}{r_p} \right) \right). \tag{16}$$

The relationship between the normal distribution and the T-distribution is as follows (Fang and Xu 2016):

$$T(0, \sigma_n^2, n = \infty) \sim N(0, \sigma_n^2). \tag{17}$$

Substituting Eq. (15) into Eqs. (9) and (10), Eqs. (18) and (19) can be obtained. Furthermore, we set $u = 0$.

$$f_{ITM} = \frac{\sqrt{2}\Gamma\left(\frac{n+1}{2}\right)}{r_p\Gamma(n/2)\sqrt{n}} \left[1 + \frac{2\pi x^2}{nr_p^2} \right]^{-\left(\frac{n+1}{2}\right)}, \tag{18}$$

$$F_{ITM} = \frac{1}{2} + \frac{\sqrt{2}x\Gamma\left(\frac{n+1}{2}\right) {}_2F_1\left(\frac{1}{2}, \frac{n+1}{2}; \frac{3}{2}; -\frac{2\pi x^2}{nr_p^2}\right)}{r_p\Gamma(n/2)\sqrt{n}}. \tag{19}$$

The following can be derived from Eq. (17):

$$f_{ITM}(n = \infty) \sim N \left(0, \left(\frac{r_p}{\sqrt{2\pi}} \right)^2 \right). \tag{20}$$

The following can be derived from Eq. (14):

$$f_{ITM}(n = \infty) = \frac{1}{r_p} \exp \left(-\pi \left(\frac{x}{r_p} \right)^2 \right). \tag{21}$$

Thus, when n is positive infinity, f_{ITM} is equivalent to the influence function w_{PIM} . Therefore, their CDFs are equivalent.

$$\lim_{n \rightarrow +\infty} F_{ITM} = F_{PIM}. \tag{22}$$

When the scope of the excavation area along the strike or dip of the coal seam is semi-infinite, the prediction equation for the surface subsidence based on the PIM can be expressed as follows:

$$W_{PIM} = \frac{W_{max}}{2} \left(1 + \operatorname{erf} \left(\frac{x\sqrt{\pi}}{r_p} \right) \right) = W_{max} F_{PIM} = W_{max} \lim_{n \rightarrow +\infty} F_{ITM}, \tag{23}$$

where W_{max} is the maximum subsidence value.

An influence function is typically the PDF of a continuous distribution function. Therefore, the influence function of the prediction model for the ITM-based surface subsidence can be expressed using Eq. (24):

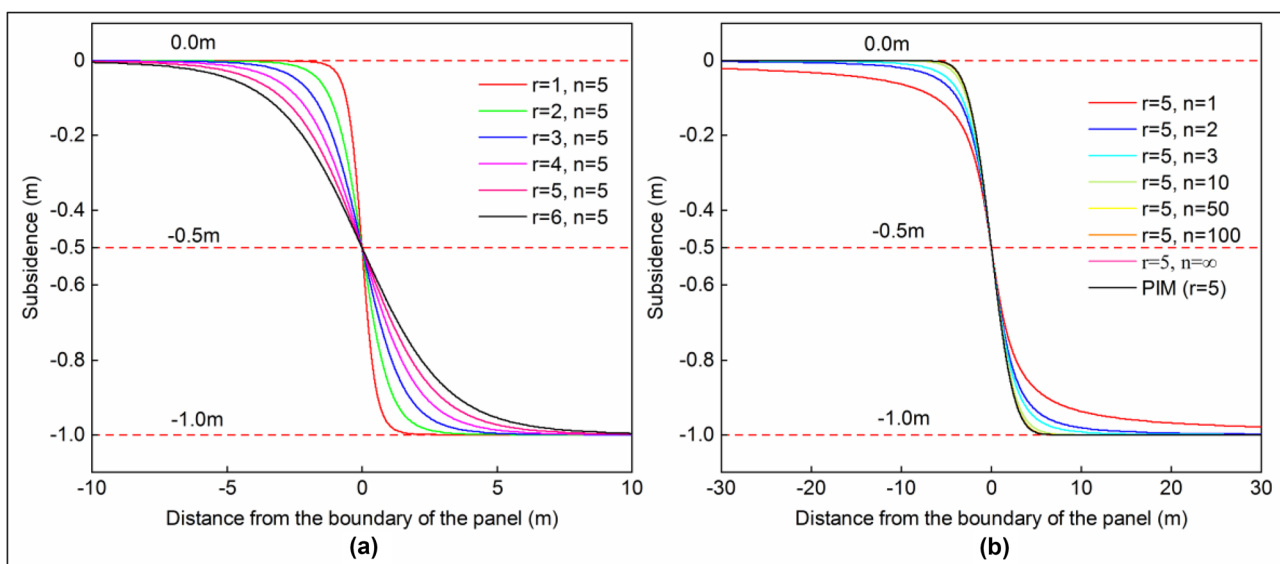


Fig. 9 Subsidence curve based on Eq. (25)

Table 7 Parameters of the ITM

<i>R</i>	<i>q</i>	$\tan\beta$	θ (°)	<i>s_z</i> (m)	<i>s_y</i> (m)	<i>s₁</i> (m)	<i>s₂</i> (m)	<i>n</i>
0.88	0.473	1.754	90	31	130	130	86	2.011
1.31	0.436	1.518	90	27	66	130	50	6.580

$$w_{ITM} = \frac{\sqrt{2}\Gamma\left(\frac{n+1}{2}\right)}{r\Gamma\left(\frac{n}{2}\right)\sqrt{n}} \left[1 + \frac{2\pi x^2}{nr^2} \right]^{-\left(\frac{n+1}{2}\right)}, \tag{24}$$

where *r* is the main influence radius.

Therefore, when the scope of the excavation area along the strike or dip of the coal seam is semi-infinite, the prediction equation for surface subsidence based on the ITM can be derived from Eq. (23), as follows:

$$W_{ITM} = W_{max}F_{ITM} = W_{max} \left(\frac{1}{2} + \frac{\sqrt{2x}\Gamma\left(\frac{n+1}{2}\right) {}_2F_1\left(\frac{1}{2}, \frac{n+1}{2}; \frac{3}{2}; -\frac{2\pi x^2}{nr^2}\right)}{r\Gamma\left(\frac{n}{2}\right)\sqrt{n}} \right). \tag{25}$$

The subsidence curve for $W_{max} = -1$ m based on Eq. (25) is shown in Fig. 9 (calculated with MATLAB and plotted with Origin).

As shown in Fig. 9, the thickness of the tail of the curve gradually increases when *r* increases or *n* decreases. Therefore, the ITM is co-regulated by *r* and *n* to change the morphology of the curve. When the main influence radii of the ITM and PIM were the same, and when *n* was positive infinity, the curves of the ITM and PIM coincided, thus proving the correctness of the derivation in this study.

As shown in Eq. (1), $W_{pim}(x, y)$ consists of the W_{PIM} . Replacing W_{PIM} with W_{ITM} in Eq. (1), the calculation equation for the subsidence of any point on the surface based on ITM is obtained analogously, as follows:

$$W(x, y) = \frac{1}{W_{max}} \left[W_{ITM}\left(x + \frac{l}{2} - s_y\right) - W_{ITM}\left(x - \frac{l}{2} + s_z\right) \right] \left[W_{ITM}\left(y - H\cot\theta + \frac{L}{2} - DS_2\right) - W_{ITM}\left(y - H\cot\theta - \frac{L}{2} + DS_1\right) \right], \tag{26}$$

$$W_{max} = Mq\cos\alpha, \tag{27}$$

$$L = \frac{D\sin(\alpha + \theta)}{\sin\theta}, \tag{28}$$

$$DS_1 = \frac{s_1\sin(\alpha + \theta)}{\sin\theta}, \tag{29}$$

$$DS_2 = \frac{s_2\sin(\alpha + \theta)}{\sin\theta}, \tag{30}$$

$$r = \frac{H}{\tan\beta}, \tag{31}$$

where *q*, $\tan\beta$, and θ denote the subsidence factor, tangent of main influence angle, and the influence transference angle, respectively; *s_z* and *s_y* denote the deviations of the inflection point on the left and right sides of the coal seam, respectively; and *s₁* and *s₂* indicate the deviations of the inflection point on the dip and rise sides of the coal seam, respectively.

In summary, there were eight ITM parameters. The physical meanings of *q*, $\tan\beta$, θ , *s_z*, *s_y*, *s₁*, and *s₂* are the same as those of the PIM parameters. In addition, the ITM has one additionally parameter than the PIM. This parameter is the degree of freedom *n*. The smaller the value of *n*, the thicker the tail of the function curve. Therefore, the ITM is theoretically suitable for predicting surface subsidence with a “long-tailed” distribution in the Hujierite mining area. Equation (23) shows that the ITM is equivalent to PIM when the other parameters are equal and *n* is positive infinity.

Effect of the fitting

The ITM was used to fit the subsidence data for the Hujierite mining area when the *R* value was 0.88 and 1.31. The fitting method used was APSO, which is the same as that of PIM. The parameters and accuracies obtained from the fit are listed in Tables 7 and 8, respectively. The effects of the fitting are shown in Fig. 10.

As shown in Fig. 10, the predicted value of the ITM was larger at the edge position of the subsidence basin compared with the PIM. Therefore, the ITM is more suitable for predicting surface subsidence with a “long-tailed” distribution in the Hujierite mining area. Moreover, the data presented in Table 8 revealed that the total fitting error of the ITM and the fitting error of the edge position of a subsidence basin were smaller than those of PIM. Essentially, when *R* was 0.88 and 1.31, the prediction accuracy of the ITM was better than that of PIM. Therefore, compared with PIM, ITM

Table 8 Comparison between the fitting error of PIM and that of ITM

<i>R</i>	ITM		PIM	
	<i>m_t</i> (mm)	<i>m_e</i> (mm)	<i>m_t</i> (mm)	<i>m_e</i> (mm)
0.88	69.9	61.1	82.6	78.1
1.31	92.9	79.4	93.7	84.3

Here, *m_t* is the total fitting error, and *m_e* is the fitting error for the edge position of the subsidence basin

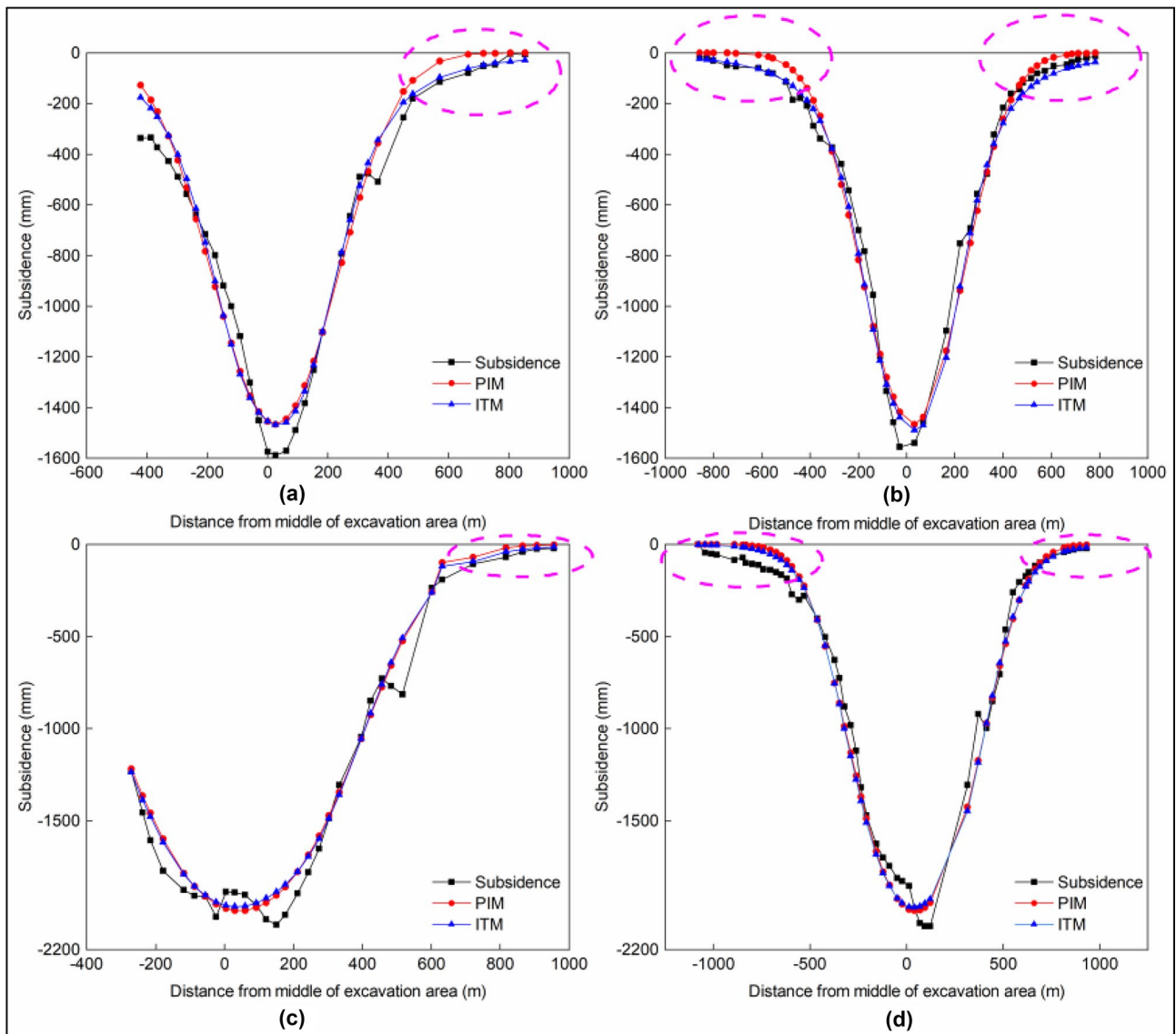


Fig. 10 Comparison between the fitting effect of PIM and that of ITM, when **a** $R=0.88$ for line A, **b** $R=0.88$ for line B, **c** $R=1.31$ for line A, and **d** $R=1.31$ for line B

can more accurately determine the boundaries of mining-induced damage, which is conducive to the protection of important buildings and structures in the mining area.

Conclusions

- (1) With an R of 0.44, 0.88, and 1.31, the subsidence factors were 0.129, 0.427, and 0.429, and the boundary angles were 55.4° , 46.4° , and 45.0° , respectively. Although the mining degree of the study area was higher than that of some coal mines in the eastern and western regions of China, the subsidence factor of the study area was still lower than that of the coal mines. Owing to several layers
- (2) In this study, the law of surface subsidence in the mining area with the advancement of a longwall panel was not investigated. In the future, we will continue to study the dynamic subsidence law in mining areas. In addition, we will continue to develop new subsidence prediction models to significantly improve the accuracy of subsidence predictions.

Acknowledgements This research was supported by the National Natural Science Foundation of China, Graduate Innovation Program of China University of Mining and Technology, and the Postgraduate Research & Practice Innovation Program of Jiangsu Province. We thank the Wushen Country Coal Bureau of the Inner Mongolia Autonomous Region of China and its affiliated coal mine enterprises and the Mining Damage and Protection Research Institute of China University of Mining and Technology for providing information on conditions of geology and mining, and key measured data of the Hujerte mining area.

Funding Funded by the National Natural Science Foundation of China (grant number 51974292); funded by the Graduate Innovation Program of China University of Mining and Technology (grant number 2022WLKXJ105); funded by the Postgraduate Research & Practice Innovation Program of Jiangsu Province (grant number KYCX22_2588).

Declarations

Competing interests The authors declare no competing interests.

References

- Cai L, Zhou HC, Bai H, Cai ZG, Yin KT, Bai YJ (2022) Application load forecasting method based on multi-layer bidirectional LSTM and improved PSO algorithm. *J. Zhejiang Univ. (Eng. Sci.)* 54(12):2414–2422. <https://doi.org/10.3785/j.issn.1008-973X.2020.12.016>
- Chen JJ (2015) Deformation mechanism and its characteristic of the surface and overburden due to high-intensity coal mining under wind-deposited sand zone. Dissertation, Henan Polytechnic University
- Chen C, Hu ZQ, Wang J, Jia JT (2019) Dynamic surface subsidence characteristics due to super-large working face in fragile-ecological mining areas: a case study in Shendong Coalfield. *China Adv Civ Eng* 2019:16. <https://doi.org/10.1155/2019/8658753>
- Chen C (2020) The theory and application of skew symmetric normal distribution. Dissertation, Yangzhou University
- Chi SS (2021) Research and application of spatio-temporal correlation model of surface movement and deformation response in deep mining. Dissertation, Anhui University of Science and Technology
- Deng KZ, Tan ZX, Jiang Y, Dai HY, Shi Y, Xu LJ (2014) Deformation monitoring and subsidence engineering, 1st edn. China University of Mining and Technology Press, Xuzhou
- Fang KT, Xu JL (2016) Statistical distribution, 1st edn. Higher Education Press, Beijing
- Finkelman RB, Tian LW (2018) The health impacts of coal use in China. *Int Geol Rev* 60(5–6):579–589. <https://doi.org/10.1080/00206814.2017.1335624>
- Fernandez PR, Granda GR, Krzemien A, Cortes SG, Valverde GF (2020) Subsidence versus natural landslides when dealing with property damage liabilities in underground coal mines. *Int J Rock Mech Min Sci* 126:13. <https://doi.org/10.1016/j.ijrmmms.2019.104175>
- Guo QB, Guo GL, Lv X, Zhang WX, Lin YK, Qin SY (2016) Strata movement and surface subsidence prediction model of dense solid backfilling mining. *Environ Earth Sci* 75(21):1426. <https://doi.org/10.1007/s12665-016-6237-6>
- Ghabraie B, Ren G, Barbato J, Smith JV (2017) A predictive methodology for multi-seam mining induced subsidence. *Int J Rock Mech Min Sci* 93:280–294. <https://doi.org/10.1016/j.ijrmmms.2017.02.003>
- Gong YQ, Guo GL (2019) A Data-Intensive FLAC(3D) Computation model: application of geospatial big data to predict mining induced subsidence. *CMES-Comp Model Eng Sci* 119(2):395–408. <https://doi.org/10.32604/cmesci.2019.03686>
- Guo KK, Guo GL, Li HZ, Wang CY, Gong YQ (2020) Strata movement and surface subsidence prediction model of deep backfilling mining. *Energ Source Part A*. <https://doi.org/10.1080/15567036.2020.1838002>
- Hu BN, Zhang HX, Shen BH (2017) Guidelines for the retention and mining of coal pillars in buildings, water bodies, railways and main shafts, 1st edn. China Coal Industry Publishing House, Beijing
- Jia XG, Song GJ, Chen K (2019) Study on influence of mining face advancing velocity on progressive surface subsidence and deformation. *Coal Sci Technol* 47(7):208–214. <https://doi.org/10.13199/j.cnki.cst.2019.07.027>
- Kwinta A, Gradka R (2020) Analysis of the damage influence range generated by underground mining. *Int J Rock Mech Min Sci* 128:104263. <https://doi.org/10.1016/j.ijrmmms.2020.104263>
- Li PX (2012) Study on regularity and prediction method of surface subsidence due to deep mining—taking Xuzhou coal mining area as example. Dissertation, China University of Mining and Technology.
- Li L, Wu K, Zhou DW (2014) AutoCAD-based prediction of 3D dynamic ground movement for underground coal mining. *Int J Rock Mech Min Sci* 71:194–203. <https://doi.org/10.1016/j.ijrmmms.2014.04.025>
- Li LY (2017) Measurement and study on law of surface subsidence occurred by fully mechanized mining of shallow coal seam with high cutting height. *Coal Technol* 36(06):25–26. <https://doi.org/10.13301/j.cnki.ct.2017.06.009>
- Liu H, Deng KZ, Zhu XJ, Jiang CL (2019) Effects of mining speed on the developmental features of mining-induced ground fissures. *Bull Eng Geol Environ* 78(8):6297–6309. <https://doi.org/10.1007/s10064-019-01532-z>
- Li HZ, Zha JF, Guo GL (2019) A new dynamic prediction method for surface subsidence based on numerical model parameter sensitivity. *J Clean Prod* 233:1418–1424. <https://doi.org/10.1016/j.jclepro.2019.06.208>
- Li ZH, Pang YK, Bao YS, Ma ZY (2020) Research on surface failure law of working faces in large mining height and shallow buried coal seam. *Adv Civ Eng* 2020:14. <https://doi.org/10.1155/2020/8844249>
- Moore DS, McCabe GP, Craig BA (2012) Introduction to the practice of STATISTICS, 7th International Edition. W. H. Freeman and Company, New York.
- Peng SS, Li HM, Zhou Y et al (2015) Research on ground control in Shendong and Zhungeer mining areas, 1st edn. Science Press, Beijing
- Salmi EF, Nazem M, Karakus M (2017) Numerical analysis of a large landslide induced by coal mining subsidence. *Eng Geol* 217:141–152. <https://doi.org/10.1016/j.enggeo.2016.12.021>
- Shen T, Zhu ZR (2019) Analysis of measured mining subsidence parameters in Northern Shaanxi mining area. *Coal Sci Technol* 47(12):207–213. <https://doi.org/10.13199/j.cnki.cst.2019.12.030>
- Tajdus K, Misa R, Sroka A (2018) Analysis of the surface horizontal displacement changes due to longwall panel advance. *Int J Rock Mech Min Sci* 104:119–125. <https://doi.org/10.1016/j.ijrmmms.2018.02.005>
- Tao YM, Jia JW, Yan JX (2021) Study and observation on surface subsidence at 3101 working face of Chahasu Colliery. *Jiangxi Coal Sci Technol* 02:160–162. <https://doi.org/10.3969/j.issn.1006-2572.2021.02.054>
- Wen Z (2015) Proficient in MATLAB intelligent algorithm, 1st edn. Tsinghua University Press, Beijing
- Wu SK (2015) The technology design of surface movement observation station – taking 1113(3) repeating working face of Zhuji east coal

- mine as an example. Dissertation, Anhui University of Science and Technology
- Wang CX, Lu Y, Shen BT, Li YY, Liang YB (2021) Design and monitoring of CPB replacement mining RSCP: a case study in China. *ENERG SOURCE PART A* 43(1):80–95. <https://doi.org/10.1080/15567036.2019.1623944>
- Xie L (2015) Pan Yi Dong Mine 1242(1) Working surface's analysis and evaluation of mining subsidence damage. Dissertation, Anhui University of Science and Technology
- Xu JL (2016) Distribution law of mining-induced strata fractures and its applications, 1st edn. China University of Mining and Technology Press, Xuzhou
- Xu JM, Zhu WB, Xu JL, Wu JY, Li YC (2021) High-intensity longwall mining-induced ground subsidence in Shendong coalfield, China. *Int J Rock Mech Min Sci* 141:104730. <https://doi.org/10.1016/j.ijrmms.2021.104730>
- Yan WT, Dai HY, Chen JJ (2018) Surface crack and sand inrush disaster induced by high-strength mining: example from the Shendong coal field. *China Geosci J* 22(2):347–357. <https://doi.org/10.1007/s12303-017-0031-7>
- Yang J, Liu J, Huang H, Liang XY (2019) Key groundwater control factors of deep buried coalfield by landform and sedimentation in the Northern Ordos Basin. *Adv Earth Sci* 34(5):523–530. <https://doi.org/10.11867/j.issn.1001-8166.2019.05.0523>
- Zhang GZ, Liu YX (2015) Research on the law of surface subsidence under the condition of large mining height and fully-mechanized coal mining technology. *Mining Surveying* 01:68–70. <https://doi.org/10.3969/j.issn.1001-358X.2015.01.23>
- Zhu ZR (2019) Study on real-time subsidence under high-intensity mining. *Coal Geol China* 31(04):68–70+84. <https://doi.org/10.3969/j.issn.1674-1803.2019.04.14>
- Zhang LL, Cheng H, Yao ZS, Wang XJ (2020) Application of the improved Knothe time function model in the prediction of ground mining subsidence: a case study from Heze City, Shandong Province. *China Appl Sci-Basel* 10(9):3147. <https://doi.org/10.3390/app10093147>

Springer Nature or its licensor holds exclusive rights to this article under a publishing agreement with the author(s) or other rightsholder(s); author self-archiving of the accepted manuscript version of this article is solely governed by the terms of such publishing agreement and applicable law.